High-resolution shallow crustal shear wave velocity structure of Anyuan mining area and its adjacent region in Jiangxi Province, China

Meng Gong[1,2,4], Jian Lv[3*] , Xingmian Zhang[4], Yong Zheng[5], Hao Chen[3], Jun Dong[3], Xiaohui Zha[3], Zheng Li[3], Shuzhong Sheng[4] and Tongli Wang[6]

Abstract

High-resolution seismic image is critically important for mining minerals. In this study, we collected seismic data from a local dense seismic array consisting of 154 stations around the Anyuan mining area and its adjacent region of Pingxiang City, Jiangxi Province in South China, and applied the ambient noise tomography (ANT) method to image the shear wave velocity structure in the study area. Shallow crustal velocities at depths less than 3.3 km were determined by direct inversion of Rayleigh wave group velocity dispersion curves at the period range of 0.5–5.0 s. Overall, the S-wave velocity structure has a tight correlation with surface geological and tectonic features in the study area. The shear wave velocity structure in the shallow crust of the Anyuan Mine and its adjacent areas displayed distinct low-velocity anomalies, which can be attributed to the depression of sedimentary structures and coal mining activities in the Pingxiang-Leping region. The zones surrounding the Anyuan fault (AYF) and Wangkeng fault (WKF) zones exhibited low-velocity anomalies from the ground surface to ~ 3.3 km underground. And the low-velocity anomalies at depths less than 1.2 km could be related to the sedimentary environment of coal mine and the coal mining activities, while the low-velocity anomalies at depths below 1.2 km are caused by the presence of fracture medium, oil and gas in the fault zone. The shear wave velocity changes sharply across the AYF, and the characteristics of the velocity change interface indicate that the AYF is inclined toward the northwest, with its extension reaching depths of approximately 3 km underground.

Keywords Anyuan mine, Ambient noise tomography, Directly surface wave tomography, Shallow crustal velocity structure, Local dense array
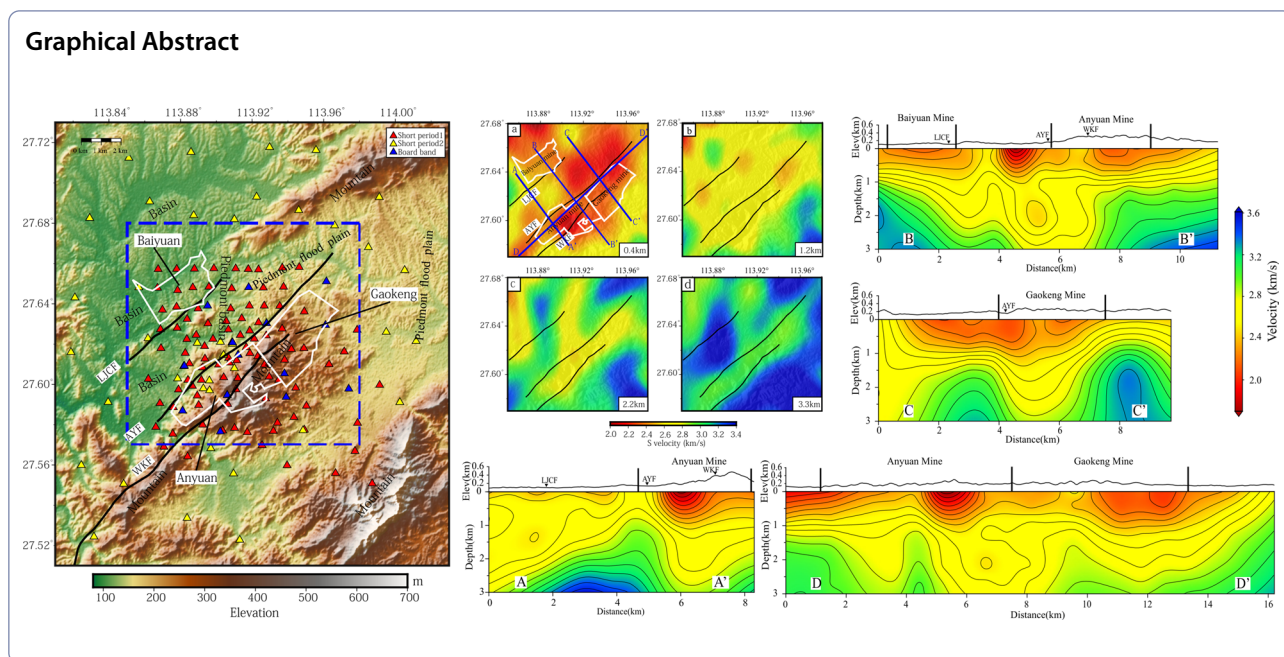
*Correspondence:
Jian Lv
lvjian8438@163.com
Full list of author information is available at the end of the article

Gong *et al. Earth, Planets and Space*   (2023) 75:129

Page 2 of 15

Graphical Abstract

Introduction

In recent decades, the ambient noise tomography (ANT) method develops quickly to image the crustal velocity structure. The basic idea of this method is to extract Empirical Green Functions (EGFs) from cross-correlations of ambient noise and coda waves between station pairs with sufficiently long records (Campillo and Paul 2003; Shapiro and Campillo 2004; Sabra et al. 2005). Based on the time reverse theory, each station can be set as a virtual source or a signal-receiving station (Cassereau et al. 1992). Therefore, this method is no longer limited by the temporal and spatial distribution of seismic events, and it is very suitable for deciphering precise crust and mantle velocity structures in low seismicity regions (Li et al. 2016a; Zhang et al. 2016; Liu et al. 2018). Benefiting from this advantage, the ANT has been widely used to image crustal and upper-mantle velocity structures at various scales (Sabra et al. 2005; Yao et al. 2006, 2008; Yang et al. 2007; Lin et al. 2007, 2008; Bensen et al. 2007, 2008; Zheng et al. 2011; Li et al. 2009, 2010, 2012).

In recent years, with the development of dense seismic array technology, the high-resolution structure of the shallow crust inversion at a small regional scale using high-frequency surface wave in ambient noise has developed significantly (Huang et al. 2010; Lin et al. 2013; Fang et al. 2015; Li et al. 2016b). Among these inversion methods, Fang et al. (2015) developed a direct surface wave imaging technology based on the typical ANT method. This technology can directly image the 3-D shear wave velocity from the surface wave dispersion between station pairs, omitting the intermediate steps of surface wave group velocity and phase velocity imaging. Moreover, the direct surface-wave tomography method takes influences of surface wave ray bending in complex medium, thus can provide a more accurate velocity structure of the shallow crust at small regional scale (Fang et al. 2015; Li et al. 2016b), and the advantages of this method have been validated by numerous tomographic studies (Wang et al. 2018; Gu et al. 2019; Xie et al. 2021; Huang et al. 2021). For instance, Wang et al. (2018) used this method imaged the shallow 3-D S-wave velocity structure of the Hutubi gas storage area in the southern margin of Junggar Basin and revealed the characteristics of near-surface structure and the gas storage. Gu et al. (2019) imaged the detailed shallow subsurface structure around the Tanlu fault zone by deploying 53 stations with an average spacing close to 5 km. Xie et al. (2021) imaged a 3-D crustal velocity structure within 5.0 km underground the mining area and provided an effective basis for exploring deep-buried gold deposits in the Qingchengzi eastern of Liaoning Province. Based on this method, Huang et al. (2021) imaged a 3-D S-wave velocity structure within 1 km underground the well field area and predicted the distribution characteristics of gas content by combining petrologic experiment in the Sijiazhuang Coal mine in Shanxi Provinces of China.

The shallow crustal structure provides fundamental clues for analyzing metallogenic mechanisms and estimating the ore reserve. The Anyuan mining area located in the western section of the Pingxiang-Leping depression in Jiangxi Province, South China (Fig. 1), which is a key coal production base of Jiangxi Province
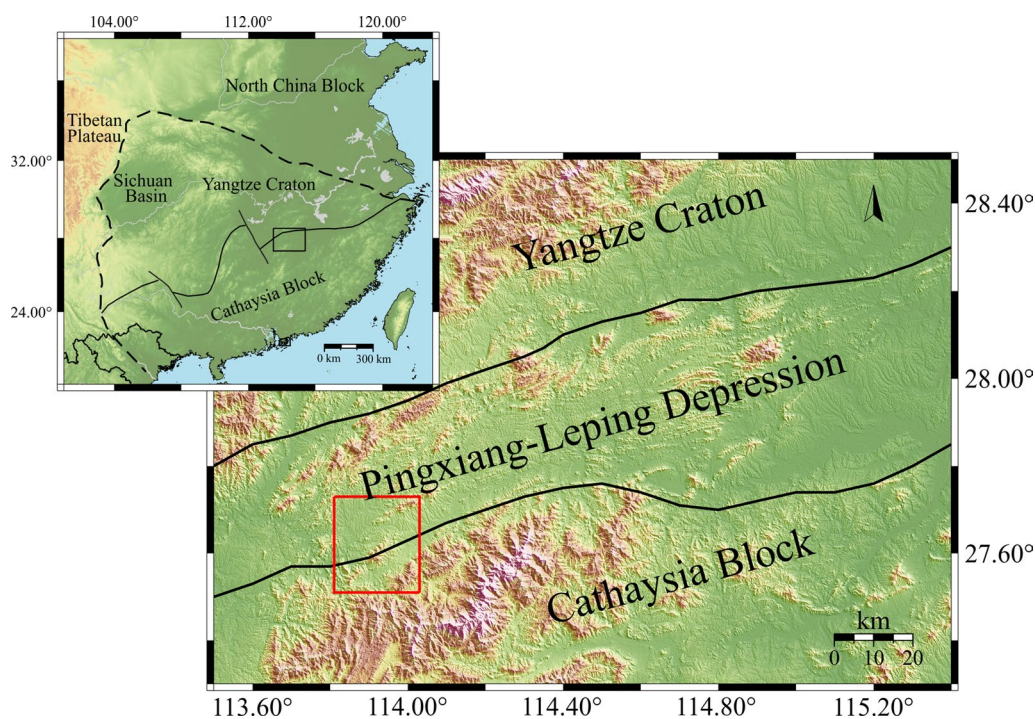
Gong *et al. Earth, Planets and Space* (2023) 75:129

Page 3 of 15

Fig. 1 Tectonic map of South China block and the Pingxiang-Leping depression areas, the bottom map is enlarged of the black rectangle area in the top map. The thick black dash line presents the boundary of the South China block and the thin black solid line is the boundary between the Yangtze Block and the Cathaysia Block in the top map (Zhang et al. 2013). The red rectangle in the bottom map corresponding the study area as shown in Fig. 2a and the black lines denote the faults

with a mining history of over a century. The Pingxiang-Leping depression is a large depression oriented in the NEE direction, bounded by deep faults on the north and south sides, and the late Paleozoic and Mesozoic strata are widely exposed. The depression exhibits a variety of facies, including marine, continental, and transitional, from the Devonian to the Paleogene. Several sets of rock source strata, primarily composed of black shale, have formed in the depression, such as Middle Permian (Xiaojiangbian Formations-Maokou Formation Nangang section), Upper Permian (Leping Formation), and Upper Triassic (Anyuan Formation) (Li et al. 2003; Deng et al. 2005). Our study region belongs to Anyuan Formation, including three mining areas, named Baiyuan, Anyuan and Gaokeng minings (Fig. 2b). Among these, only the Anyuan mining area is currently operational (Xiao 2020). There are three NE-trending reverse faults distributed in the study region, named Luojiachong fault (LJCF), Anyuan fault (AYF), and Wangkeng fault (WKF) (Tan et al. 2001).

Currently, there are no dangerous rock, collapse, landslide, and other adverse geological phenomena in the mining area (Liu et al. 2021). However, due to the problems of resource exhaustion, gas leakage, ground fissures, ground collapse, and mine earthquake in century-old

mine, it is particularly urgent to understand the 3-D structure of the shallow crust of the Anyuan Mining area and its adjacent region. Although Li et al. (2015) have studied the 3-D crustal velocity structure of Jiangxi Province, the detailed velocity structure of the shallow crust around the Anyuan mining area needs further investigation.

Therefore, it is essential to develop a high-resolution image of the shallow structure in the Anyuan mine region is of critical importance. In this study, we apply the direct surface-wave tomography method (Fang et al. 2015) to image the 3-D shear wave velocity structure of the shallow crust in Anyuan mining area and its adjacent region based on a local dense array, and our results could provide a significant scientific basis for coal mine resources exploring and seismic structure modeling.

Data and method

Data collection and processing procedure

The vertical component continuous data from 154 seismic stations around the Anyuan mining area (Fig. 2a) deployed by East China University of Technology and the Jiangxi earthquake Agency between 27 July 2020 and 31 August 2020 are used in this study. This temporary dense seismic array consists of 13 broadband seismographs of
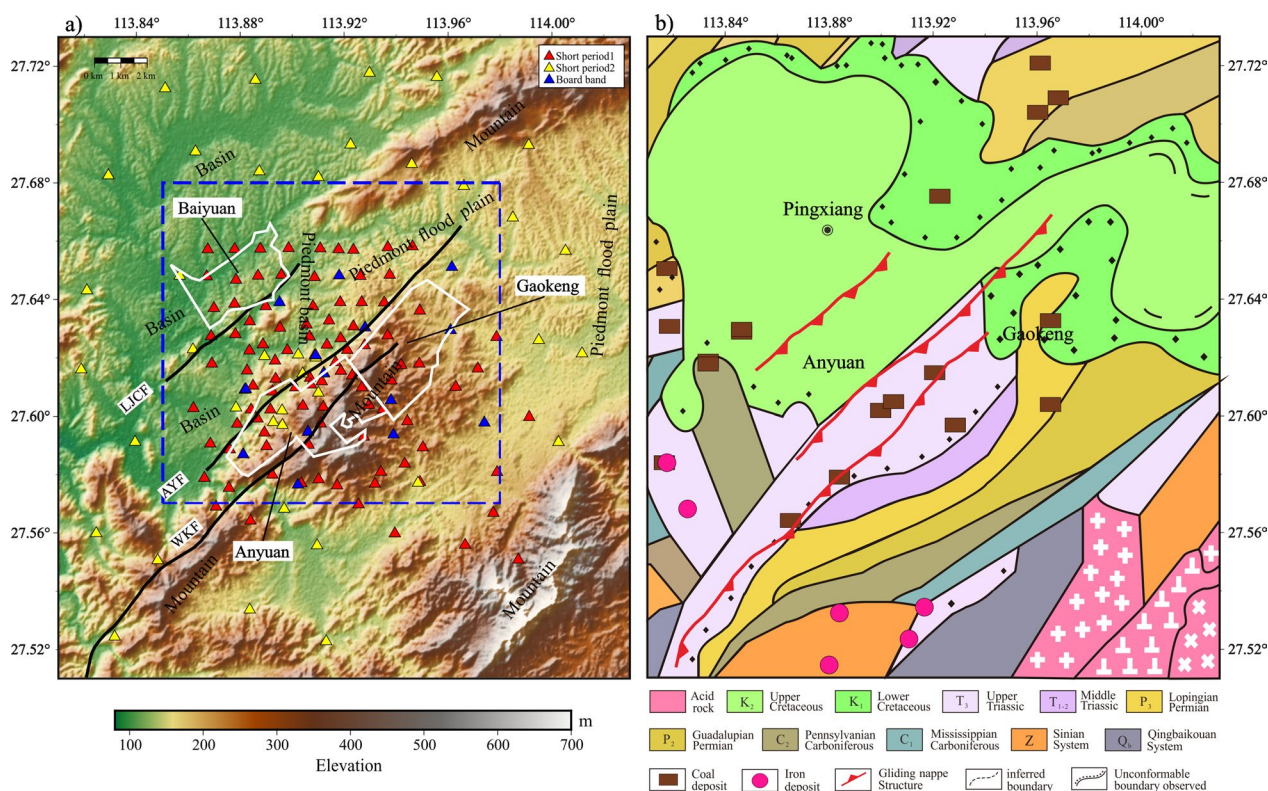
Gong *et al. Earth, Planets and Space*   (2023) 75:129

Page 4 of 15

Fig. 2 The distribution of seismic stations and the geological map of the study area. **a** The three different types of seismic instrument (GL-PCS60, EPS, and QS-05A) locations are shown as the blue, red, and yellow triangles, respectively. White closed lines represent the distributions of Anyuan, Baiyuan, and Gaokeng mining exploitation areas (advised from Xiao 2020). The main region of the inversion result is given by the blue dotted square. The black lines denote the three main faults in the study region (according to the 1:200,000 Pingxiang fault of Jiangxi Province). **b** The geological background of the Anyuan mining area and its adjacent region. The brown rectangle denotes major coal deposits (modified according to the 1:1,000,000 East China geological map and 1:500,000 Jiangxi Province geological map from http://www.ngac.cn/). (For interpretation of the references to color in this figure legend, the reader is referred to the web version of this article.)

GL-PCS60 type (the blue triangles in Fig. 2a), 98 short-period seismographs of EPS type (the red triangles in Fig. 2a), and 43 short-period seismographs of QS-05A type (the yellow triangles in Fig. 2a). The seismic array spans an area of about 18 km × 18 km with an average station spacing of about 1 km in the center area and the minimum station spacing is ~ 0.5 km. The collected data sets are recorded with a simple rate of 100 Hz.

The data processing procedure follows the methodology proposed by Bensen et al. (2007). Seismograms are first cut into daily segments. After the removal of the mean, trend, and instrument response, a 0.5–10 s band-pass filter is applied. To reduce the effect of earthquakes and instrumental irregularities on cross-correlations, the seismograms are normalized using a time–frequency normalization method (Ekström et al. 2009; Shen et al. 2012). Then daily cross-correlations for each station pair are calculated and these are stacked using the normalized linear stacking method to obtain cross-correlation functions (CCFs). Finally, the

empirical green functions (EGFs) are derived from the time derivative of the CCFs (Sabra et al. 2005; Yao et al. 2006).

Theoretically, surface wave signals should appear symmetrically on both the causal and acausal time lags of the EGFs. However, the uneven and varied spatial distribution of noise sources can affect the EGFs and make the signal emerge on the positive and negative time lags asymmetric (Stehly et al. 2007; Zhan and Clayton 2010). Therefore, to enhance the signal-to-noise ratio (SNR), the EGFs are reversed and stacked to create a symmetric component before the dispersion measurement extraction (Yang et al. 2007; Yao et al. 2011). Figure 3a illustrates the path distribution of the station pairs between the L124 station and other stations. Figure 3b displays the CCFs of station pairs with 0.5–5 s band-pass filtered and aligned by the station-pair distance. The fundamental order signals of the Rayleigh wave were clearly observed, and the surface wave group velocity ranges from approximately 1.7 to 3.6 km/s (Fig. 3b).
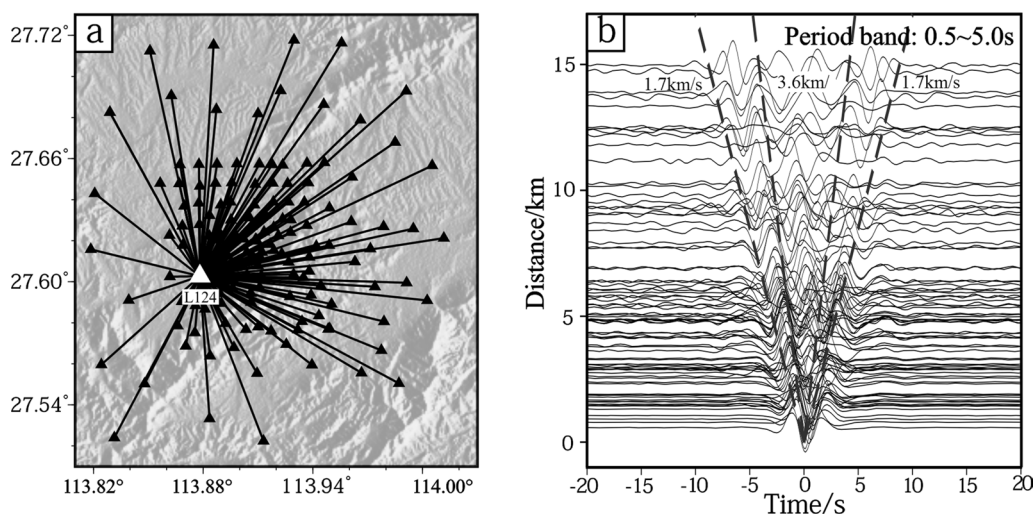
Gong *et al. Earth, Planets and Space*   (2023) 75:129

Page 5 of 15

Fig. 3 Cross-correlation functions between station L124 and other stations. **a** Ray-path coverage map between station L124 and other stations, respectively. **b** Shows cross-correlation functions with 0.5–5 s band filter between station L124 and other stations, the dash inclined lines denote the ranges of velocity (1.7 to 3.6 km/s)

Surface wave dispersion curve extraction

In general, when using the ANT method to image the surface wave velocity structure over a long time period, the inter-station distance of at least three wavelengths is required to obtain reliable frequency dispersion curves (Yao et al. 2006; Zheng et al. 2008). Yao et al. (2011) and Luo et al. (2015) demonstrated that dense seismic arrays can yield accurate dispersion curves in short-period surface wave inversion, even when the inter-station distance is only one times the wavelengths. So, we use multiple filtering techniques (Dziewonski et al. 1969; Yao et al. 2011) to extract the high-quality dispersion data from the EGFs with inter-station distances

greater than one wavelength and SNR > 5. The SNR was defined as the ratio of the maximum amplitude of the signal window of EGFs (− 15 to ∼ 15 s) and the average absolute amplitude of the noise window (− 30 to ∼ − 15 s and 15 to ∼ 30 s).

Furthermore, we removed the measurements that exceed the average value of group velocity at each period plus or minus 0.5 km/s and eliminated the data points with too high or negative slopes. Ultimately, we retained 4538 high-quality group velocity dispersion curves out of the 11,781 theoretically available dispersion curves from 154 seismic stations (Fig. 4). Figure 4 illustrates the variation of surface wave group velocity
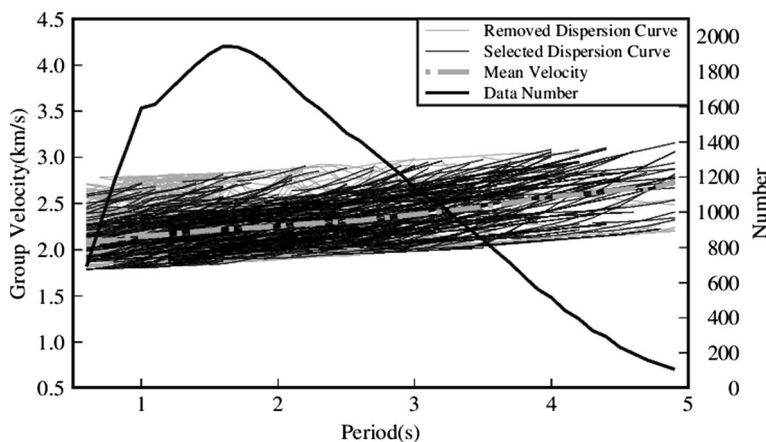

Fig. 4 Group velocity dispersion curves extract from the EGFs. The black thin solid lines denote the selected group velocity dispersion curves and the gray thin solid lines denote the removed dispersion curves. The black thick solid line shows the number of the dispersion at each period and the thick gray dashed line presents the average group velocity dispersion curve
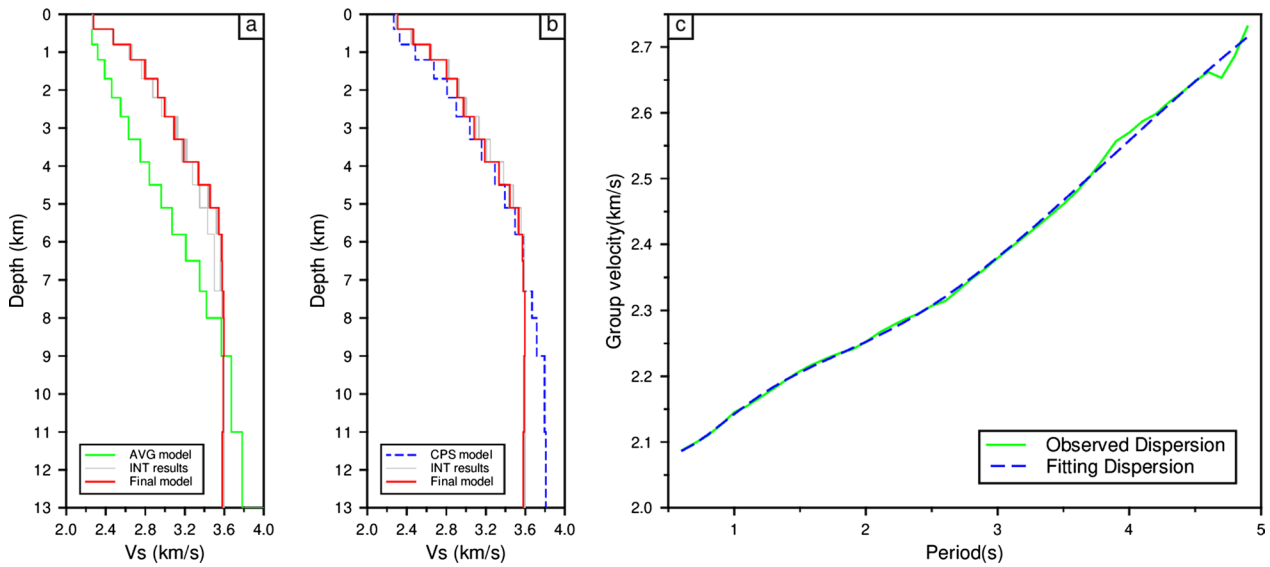
Gong *et al. Earth, Planets and Space*   (2023) 75:129

Page 6 of 15

Fig. 5 Comparison of inversion results of different initial models. **a** The green line represents the AVG model deduced from the average dispersion curves. The gray lines and the red line represent the intermediate iteration and the final model of the inversion. **b** The blue dashed line represents the CPS model computed from the CPS330 inversion. The gray and red lines represent the intermediate iteration and the final model of the inversion, respectively. **c** The fitting situation of the observed dispersion curve (green line) and the fitting dispersion curve (blue dashed line)

ranging from approximately 1.8 to 3 km/s, with the majority of periods distributed between 0.6 and 3.5 s.

Shear wave velocity structure inversion

We use the direct surface wave tomography method (Fang et al. 2015) to directly invert the mixed path Rayleigh wave group velocity dispersion data into a 3-D velocity structure. This method first assumes an initial 3-D velocity model and then performs surface wave ray tracing at each period using a fast marching method (Rawlinson and Sambridge 2004) and iteratively update the sensitivity kernels of period-dependent dispersion measurements to updates of the 3-D velocity model. To mitigate the impact of the uneven path coverage, a wavelet-based sparsity-constrained seismic tomography method (Simons et al. 2011; Fang and Zhang 2014) is employed in the 3-D wave velocity inversion.

As is well-known, the essence of inversion is to find a model m that minimizes the differences $\delta t_i(\omega)$ between the observed arrival times $t_i^{obs}(\omega)$ and theoretical arrival time $t_i(\omega)$ for all frequencies ω. The travel-time perturbation for the path i at frequency ω is expressed by Fang et al. (2015) as Eq. (1):

$$\delta t_i(\omega) = t_i^{\text{obs}}(\omega) - t_i(\omega) = -\sum_{k=1}^{K} v_{ik} \frac{\delta C_k(\omega)}{C_k^2(\omega)}, \quad (1)$$

where $t_i(\omega)$ denote the calculated travel-time using a reference model that can be updated in the inversion, and $C_k(\omega)$ and $\delta C_k(\omega)$ present the phase velocity and its perturbation of the kth grid node at the angular frequency ω, respectively. v_{ik} is the bilinear interpolation coefficients along the ray-path associated with the ith travel-time data.

Generally speaking, surface wave dispersion is most sensitive to shear wave velocity (β), but short-period Rayleigh wave dispersion is also very sensitive to compressional wave velocity (α) in shallow crust. Therefore, when we use the empirical formula (Brocher 2005) to relate the compressional wave velocity and mass density (ρ) to the shear wave velocity, Eq. (1) can be rewritten to Eq. (2) as Fang et al. (2015) described:

$$\delta t_i(w) = \sum_{k=1}^{K} (-\frac{v_{ik}}{C_k^2(\omega)}) \sum_{j=1}^{J} [R_\alpha(Z_j) \frac{\partial C_k(\omega)}{\partial \alpha_k(z_j)}$$
$$+ R_\rho(z_j) \frac{\partial C_k(\omega)}{\partial \rho_k(z_j)} + \frac{\partial C_k(\omega)}{\partial \beta_k(z_j)}]\big|_{\Theta_k} \delta \beta_k(z_j) \quad (2)$$
$$= \sum_{l=1}^{M} G_{il} m_l,$$

where Θ_k present the 1-D initial model at the kth surface grid point on the surface and $\alpha_k(z_j)$, $\beta_k(z_j)$, and $\rho_k(z_j)$ are the compression wave velocity, shear wave velocity, and mass density at the jth depth grid node, respectively. R_α and R_β present the scaling factor, and J is the number of grid points in the depth direction. The total grid points

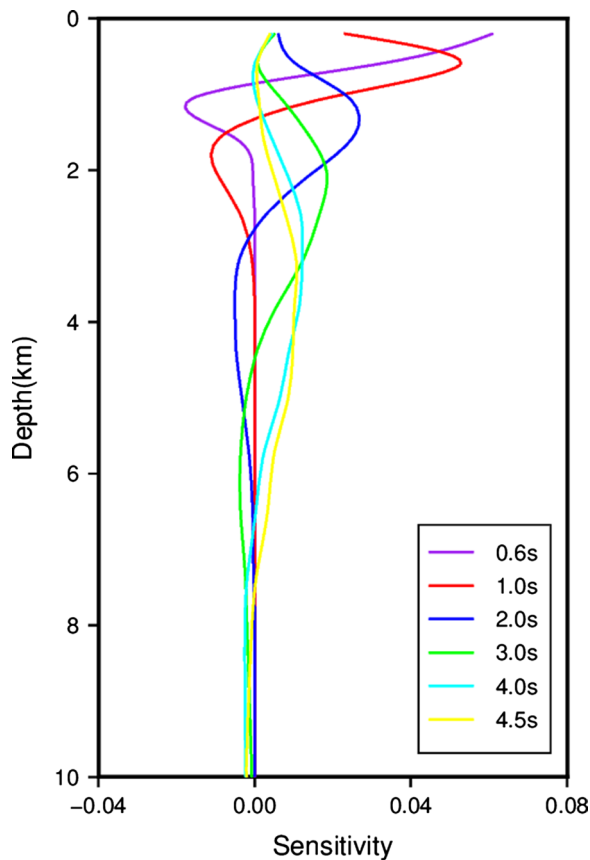Gong *et al. Earth, Planets and Space*   (2023) 75:129

Page 7 of 15

Fig. 6 Depth sensitivity kernel functions at periods of 0.6, 1.0, 2.0, 3.0, 4.0, and 4.5 s for the fundamental Rayleigh wave group velocity calculated from the CPS model in Fig. 4b

number of the 3-D model is $M = KJ$. Thus, Eq. (2) can be written in the matrix form as Eq. (3):

$$d = Gm, \tag{3}$$

where d is the travel-time residual, G is the data sensitivity matrix, and M is the model parameter. Equation (3) can be solved by minimizing the following loss function:

$$\Phi(m) = \left\| d - Gm \right\|_2^2 + \lambda \| Lm \|_2^2, \tag{4}$$

where the first term on the right-hand side gives the l_2-norm data misfit and the second term denotes the l_2-norm model regularization term. L is the model smoothing factor and λ is the weight factor of data fitting and model regularization (Simons et al. 2002; Aster et al. 2013). Thus, the solution m can be deduced from following equation (Paige and Saunders 1982a, 1982b):

$$\tilde{m} = (G^T G + \lambda L^T L)^{-1} G^T d. \tag{5}$$

To obtain a robust initial model, two methods are used to determine the 1-D mean velocity model. The first one is based on empirical formulas (Shearer et al. 2009; Fang et al. 2015), which involved using 1.1 times the average measured group velocities at a depth of 1/3 times the wavelength as the velocity model (Fig. 4a, hereafter, called AVG model). Subsequently, the AVG model is used as the input model and the iteratively damped least square method developed by Herrmann and Ammon (2002) in the CPS330 package (Herrmann 2013) is applied to obtain the other 1-D velocity model (Fig. 4b, hereafter, called CPS model). After that, the AVG and CPS models are used as the initial models for the direct 3-D surface wave inversion program to calculate the 1-D mean shear wave velocity model, respectively (Fig. 5).

Despite the significant differences between the two input models (AVG and GPS models), the inversion results were found to be essentially the same (Fig. 5a, b). This suggests that the two velocity models have minimal impact on the inversion results in this study. Previous studies by Yu et al. (2020) and Xie et al. (2021) have also proved that short-period surface wave inversion has relatively low dependence on the initial model. Thus, in view of the smaller difference between the CPS model and the inverse model, the CPS velocity model is selected as the initial model for the direct 3-D surface wave velocity structure inversion. Figure 5c shows the fitting of the dispersion curve (solid black line) and the original dispersion curve (black circle).

In the direct inversion method, the weighting factor λ in Eq. (4) is particularly important in the residual term of the data measurement and the regularization term of the model (Paige and Saunders 1982a, 1982b). If the λ is too small, the result may be over-fitted and the error will increase. Conversely, if the λ is too large, the inversion model will be excessively smooth, making the inversion result highly reliant on the initial model (Luo et al. 2019). Hence, the L-curve analysis method (Hansen 2007) is used to determine the optimal λ, and the result reveals the optimal weighting factor λ is 3.

During the inversion process, the depth sensitivity kernel is used to assess the sensitivity of surface wave group velocity on shear wave velocity in the depth direction (Yao et al. 2008; Zheng et al. 2008). Figure 6 displays the depth sensitivity kernel functions at periods of 0.6, 1.0, 2.0, 3.0, 4.0, and 4.5 s for the fundamental Rayleigh wave group velocity calculated from the CPS model as shown in Fig. 5b. It can be observed that the surface wave dispersion data between 0.6 and 4.5 s have the capability to resolve depths down to ∼ 5 km underground.
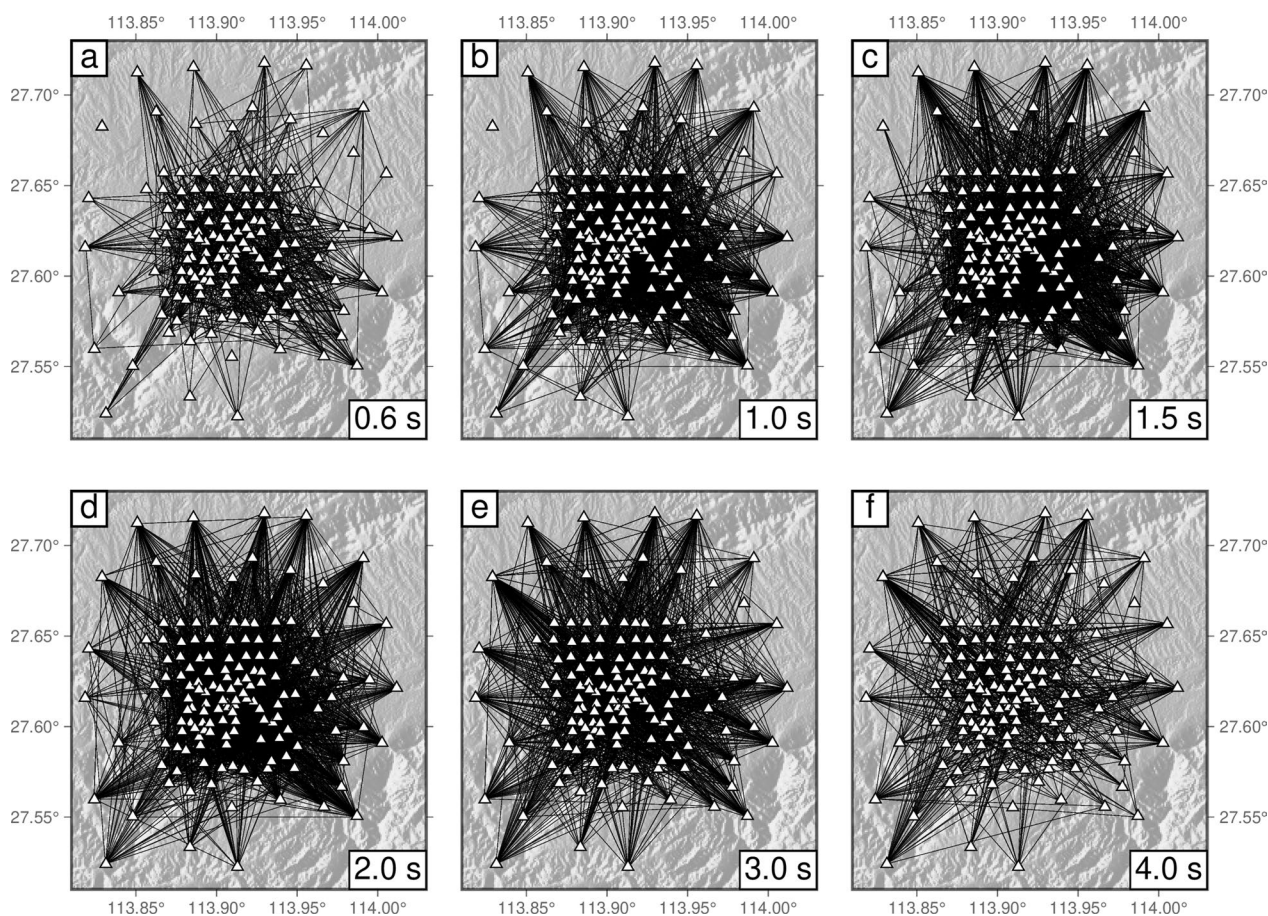
Gong *et al. Earth, Planets and Space* (2023) 75:129

Page 8 of 15

Fig. 7 Ray-path coverage maps of Rayleigh wave group velocity measurement from the final 3-D model at different periods

Results and discussion

To enhance the robustness of the 3-D shear wave inversion results, the checkerboard resolution tests are performed to assess the lateral and vertical resolutions. Theoretically, the recovery ability of the checkerboards depends primarily on the coverage of surface-wave raypath. Thus, we first check the ray-path coverage at different periods and then performed the checkerboard resolution test. Figure 7 illustrates the ray-path coverage of group velocity measurements at six selected periods, obtained from the final velocity model. The results indicate that the study region has a relatively high density of surface-wave ray-path coverage, suggesting that the structure of the region can be well imaged by the data set. We also observe that the ray-path number decreases with increasing period, such as the number of the ray-path at 4 s period is only about 27% of that at 1.5 s period.

To assess both the lateral and vertical resolution, we use a 3-D checkerboard model. The 3-D reference velocity model is constructed based on the CPS model as shown in Fig. 5b. After several comparative tests, the study region is meshed with 25 by 25 grid points with an interval of 0.01° in latitude and longitude. And 18 grid nodes are set along the depth direction from the ground surface to 13 km underground, according to the interface depth of the velocity structure. For the lateral resolution test, the anomaly size is approximately 0.025° × 0.025°, while for the vertical resolution tests, the grid size is 0.025° along the horizontal direction, gradually increasing along the vertical direction with increasing crustal depth, ranging from approximately 0.8 km to 1.5 km. Figure 8a–d shows the recovery results of the lateral checkerboard at depths of 0.4, 1.2, 2.2 and 3.3 km. The surface locations and the inverted results of vertical profiles MM' and NN' are shown in Fig. 8d and Fig. 8f, h. The recovery results indicate that the recovery of the detection board is influenced by the density of ray-path coverage. The checkerboard test is well recovered in the area with dense ray-path coverage, while the recovery is poor in the area with poor ray-path coverage. Overall, the results suggest that the structures of the Anyuan mine and its adjacent

Gong *et al. Earth, Planets and Space*   (2023) 75:129

Page 9 of 15
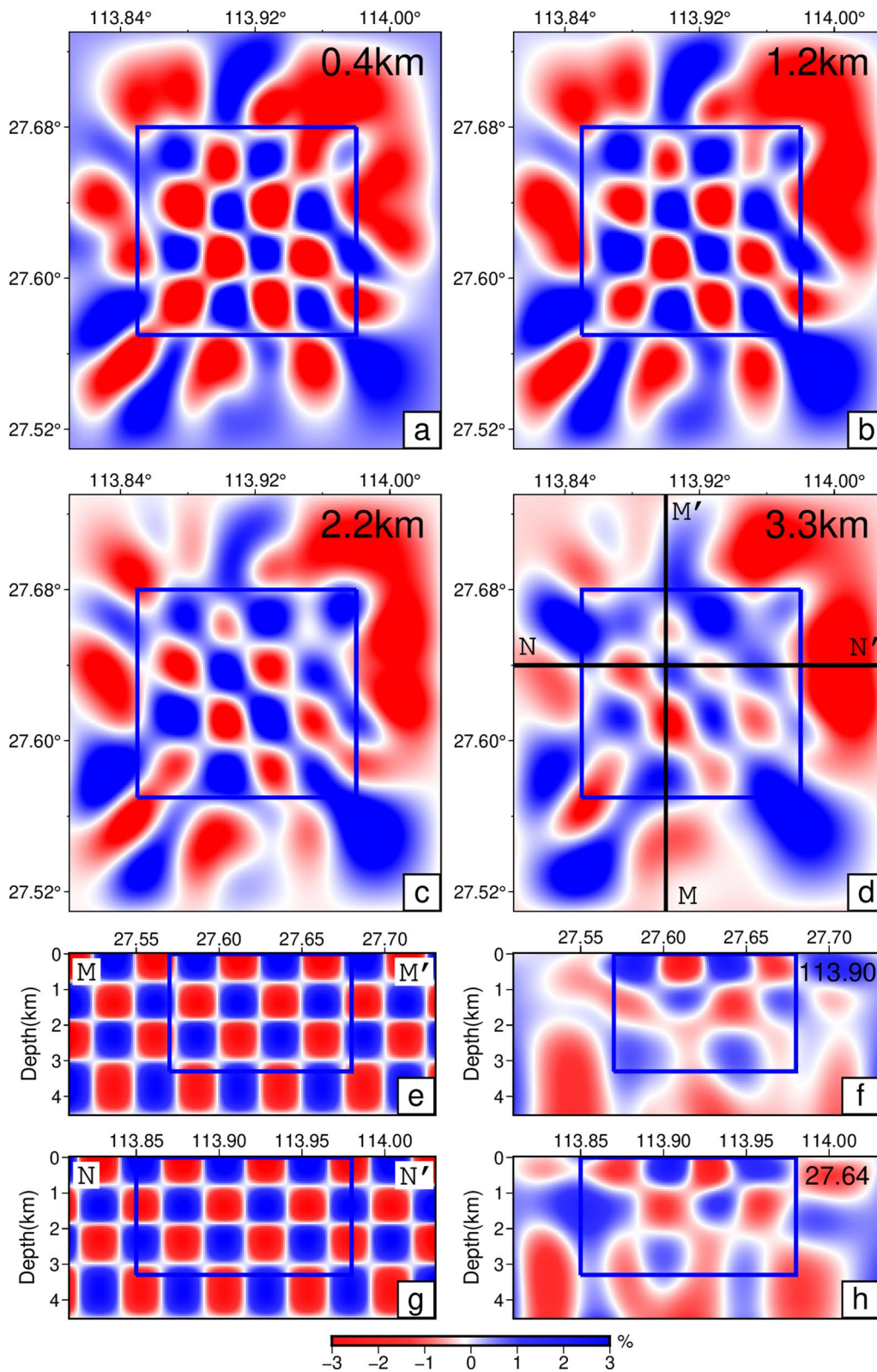
Fig. 8 Lateral and vertical checkerboard resolution tests. The lateral checkerboard test at 0.4, 1.2, 2.2 and 3.3 km depths are shown in **a**–**d**, in which the anomaly size is approximately 0.025°×0.025° in the study area (blue square). The vertical checkerboard test along latitude and longitude are shown in **e**–**h** and the location of the two profiles show in the (**a**). **e** and **g** are the checkerboard theoretical model, **f** and **h** are the vertical chessboard recovery

Gong *et al. Earth, Planets and Space* (2023) 75:129

Page 10 of 15
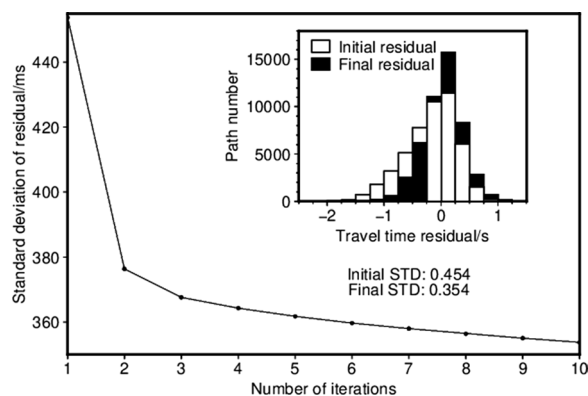

Fig. 9 Variation of the standard deviation of residual errors of surface-wave travel-time with 10 iterations of the CPS model. The insert image on the upper right corner is the distribution of the residuals

regions from the ground surface to ~3.3 km underground can be resolved well.

During the inversion process, we use the same velocity model and the parameters as those in the checkerboard resolution test. The inversion process is relatively stable and the standard deviation of residual error (STD) of surface-wave travel-time decreasing as the number of iterations times increased (Fig. 9) The STD decreases rapidly during the first three iterations, followed by a slower decrease until convergence. After 10 times iterations, the average travel-time residuals decreased from 0.454 s to 0.354 s, indicating the final velocity model fits the observed data better.

The coal-bearing strata in the study region belong to the Anyuan Formation of the Upper Triassic, which can be divided into Zijiachong member, Sanjiachong member, and Sanqiutian member from bottom to top (Fig. 10). The lithofacies assemblages of the Anyuan Formation consist mainly gray to light gray, light purple sandstone, siltstone, sandy shale, and carbonaceous shale (Li et al. 2016c). And the sedimentary environment is primarily marine–continental transitional facies and the coal seams exhibit multiple layers, complex structures, and uneven distribution (Liu and Chen 2021).

Figure 11 shows the shear wave velocity structure at different depths obtained from group velocity dispersion data through the direct surface inversion. The patterns reveal significant variations in shear wave velocity structure at the same depth, indicating strong lateral heterogeneity in the shallow crustal structure of the study region. At the depth of 0.4 km underground, the basin and coal mining areas show low-velocity anomalies, while the uplifted mountain areas without coal mine distribution exhibit high-velocity anomalies. The low-velocity anomalies in the basin areas can be attributed to

the sedimentary layer on the ground surface, while the high-velocity anomalies in the uplifted mountain areas indicate missing sedimentary layers or exposed bedrock. However, the Anyuan mine area located in the uplifted mountainous, exhibits low-velocity anomalies in its shear wave velocity structure. This abnormal phenomenon could be related to the sedimentary environment of coal seam and coal mining activities. The Anyuan mining area and its adjacent regions have a sedimentary environment characterized by the interaction of marine and continental facies with sedimentary basins, containing significant amounts of sand and silt (Xi et al. 1999; Li et al. 2003). Additionally, the Anyuan coal mine has a mining history of over one hundred years, resulting in the production of a large amount of coal mine gob area and coalbed methane during the mining process (Li et al. 2003; Qiu and Li 2019). All these factors contribute to the presence of low-velocity anomalies in the shear wave velocity structure of the Anyuan mine area.

The distribution of shear wave velocity structure in the depth ranges of 1.2–2.2 km exhibits similar characteristics. The Anyuan and Gaokeng mining areas still show low-velocity anomalies, but the ranges of the anomalies decrease with the increase of depths, gradually approaching the WKF and AYF zones. It is also observed that the shear wave velocity around the AYF zone and the piedmont basin forms a distinct "Y-shaped" zone of low-velocity anomalies. Overall, in the depth ranges of 0.4–1.2 km underground, the shear wave velocity in the entire Anyuan mining area exhibits significant low-velocity anomalies. However, at a depth of 2.2 km underground, the shear wave velocity structure of the Anyuan mining area is bounded by the WKF zone. The shear wave velocity structure in the northern part of the mining area still presents low-velocity anomalies, while the southern part gradually transitions to high-velocity anomalies, consistent with the distribution characteristics of shear wave velocity structure in high mountain areas.

At the depth of 3.3 km underground, the shear wave velocity structure is well consistent with the surface and topographic features. Mountainous areas with high terrain, such as the areas between the LJCF and AYF belts and the southern part of the WKF belt exhibit high-velocity anomalies, while basins and piedmont basins exhibit low-velocity anomalies. It is worth noting that despite the high elevation of the AYF and WKF zones, there are still low-velocity anomalies in the shear wave velocity structure around the fault zones. Previous studies on the Pingxiang-Leping depression in Jiangxi Province have shown that there are abundant Coalbed methane resources beneath the Anyuan mining area and its adjacent region (Li et al. 2003; Qiu and Li 2019).
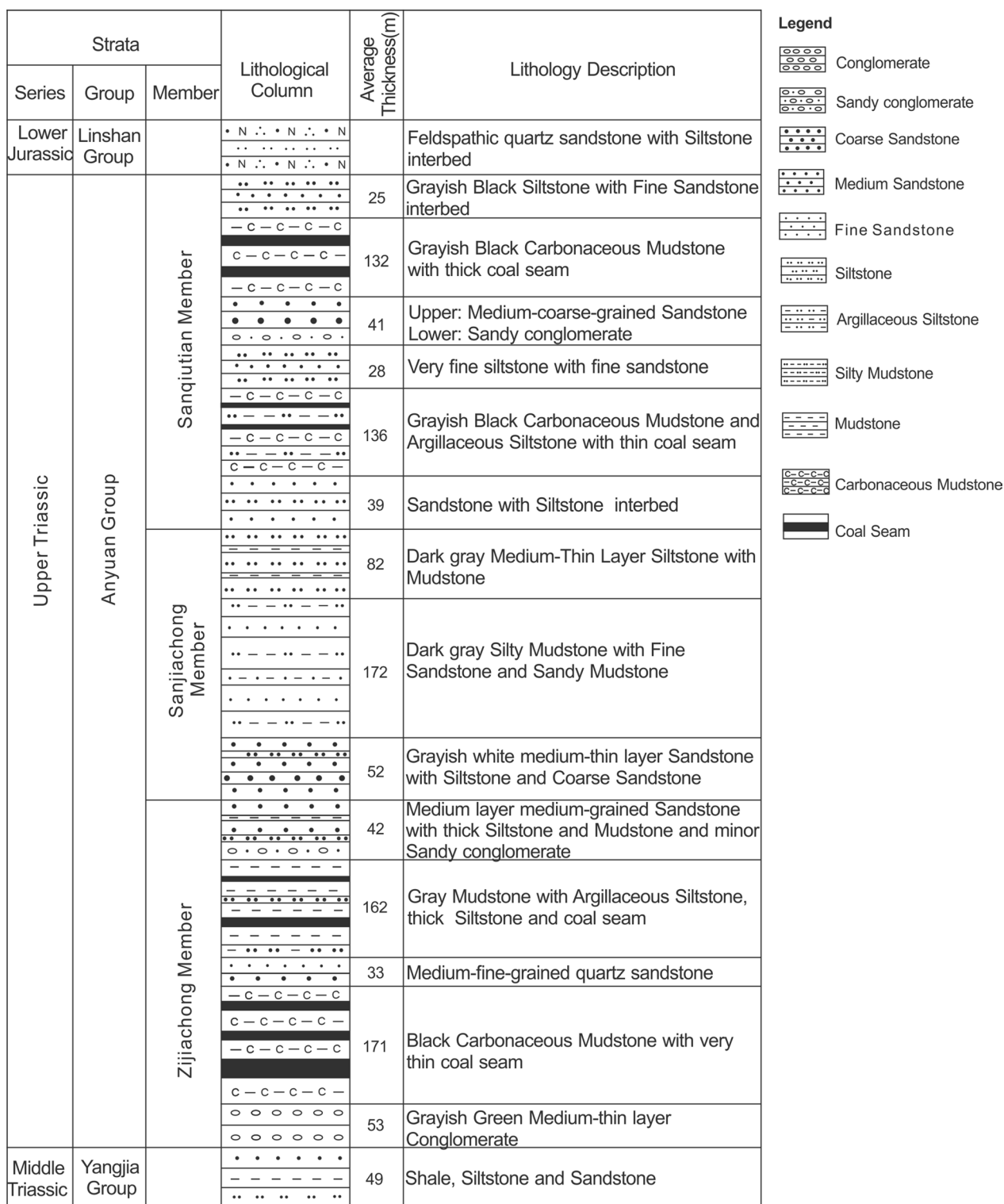
Strata			Lithological Column	Average Thickness(m)	Lithology Description
Series	Group	Member			
Lower Jurassic	Linshan Group				Feldspathic quartz sandstone with Siltstone interbed
Upper Triassic	Anyuan Group	Sanqiutian Member		25	Grayish Black Siltstone with Fine Sandstone interbed
				132	Grayish Black Carbonaceous Mudstone with thick coal seam
				41	Upper: Medium-coarse-grained Sandstone Lower: Sandy conglomerate
				28	Very fine siltstone with fine sandstone
				136	Grayish Black Carbonaceous Mudstone and Argillaceous Siltstone with thin coal seam
				39	Sandstone with Siltstone interbed
		Sanjiachong Member		82	Dark gray Medium-Thin Layer Siltstone with Mudstone
				172	Dark gray Silty Mudstone with Fine Sandstone and Sandy Mudstone
				52	Grayish white medium-thin layer Sandstone with Siltstone and Coarse Sandstone
		Zijiachong Member		42	Medium layer medium-grained Sandstone with thick Siltstone and Mudstone and minor Sandy conglomerate
				162	Gray Mudstone with Argillaceous Siltstone, thick Siltstone and coal seam
				33	Medium-fine-grained quartz sandstone
				171	Black Carbonaceous Mudstone with very thin coal seam
				53	Grayish Green Medium-thin layer Conglomerate
Middle Triassic	Yangjia Group			49	Shale, Siltstone and Sandstone

Legend

- Conglomerate
- Sandy conglomerate
- Coarse Sandstone
- Medium Sandstone
- Fine Sandstone
- Siltstone
- Argillaceous Siltstone
- Silty Mudstone
- Mudstone
- Carbonaceous Mudstone
- Coal Seam

Fig. 10 Comprehensive bar chart of Anyuan Formation in Pingxiang-Leping Depression (advised from Li et al. 2016c)
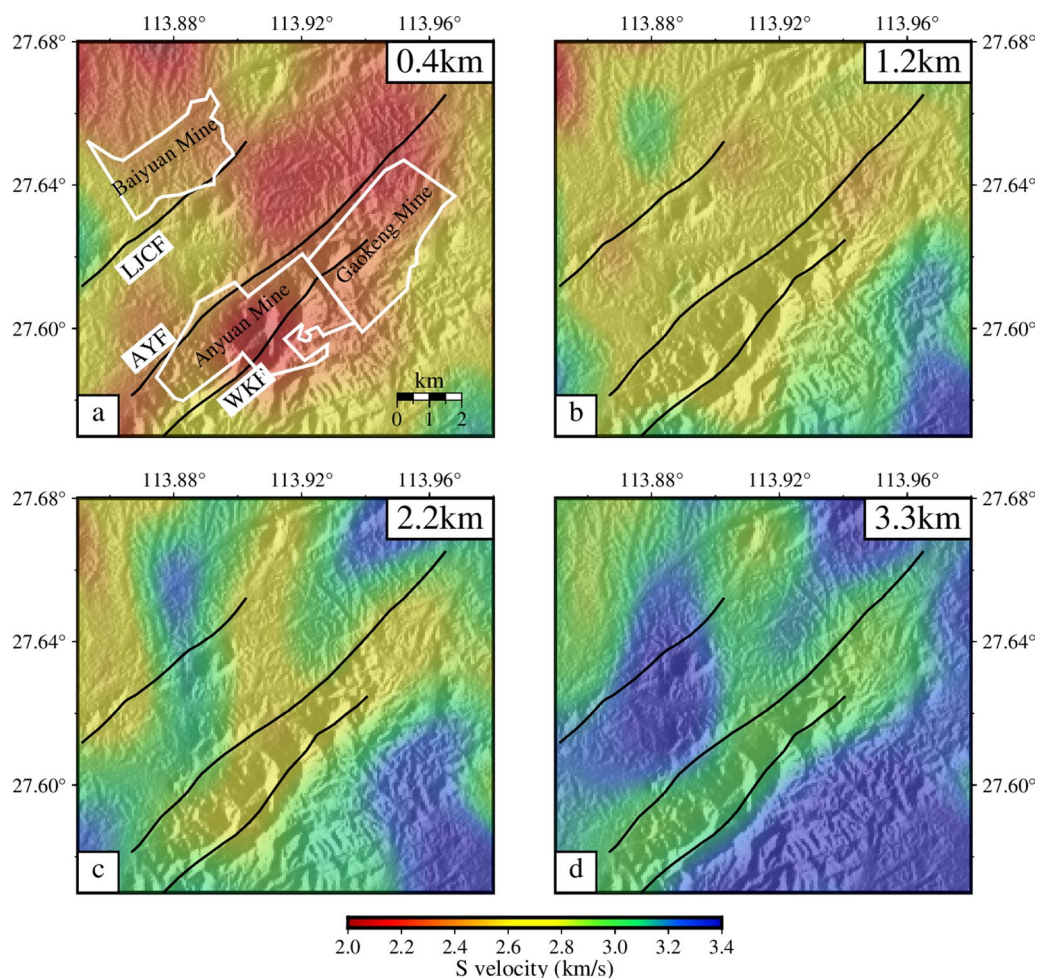
Fig. 11 Shear wave velocity slices at different depths: **a** 0.4 km, **b** 1.2 km, **d** 2.2 km, **f** 3.3 km. Black lines are the three main faults in the study area. White closed lines represent the distribution of mining exploitation areas

Therefore, the low-velocity anomalies observed at depths below 2 km around the AYF and WKF regions may indicate the presence of oil and gas between the fault zones.

Figure 12 shows the positions of the four sections and their corresponding shear wave velocity profiles. The AA' profile shows that the basin areas to the west of the AYF exhibit low-velocity anomalies, and the depths of these anomalies are negatively correlated with the surface elevation. Along the profiles AA' and CC', there is a sharp change in the shear wave velocity structure across the AYF zone, with the velocity transition interface inclined towards the northwest, consistent with the trend of the AYF (Tan et al. 2001; Liu et al. 2004). The velocity transition interface reaches depths of approximately 3 km underground, which may indicate the extension depth of the AYF. The BB' and CC' profiles show a noticeable low-velocity anomaly on the northwest side of the AYF, possibly caused by the presence of sediment and debris in the piedmont floodplain (Tan et al. 2001; Li et al. 2016c),

which significantly reduces the propagation speed of shear waves.

Along the AA', BB', CC' and DD' profiles, it can be seen that the shear wave velocity structure in the shallow surface layer (< 1.2 km) presents low-velocity anomalies, which could be related to the sedimentary environment of the coal seam. Xi et al. (1999) and Li et al. (2003) have suggested that the Anyuan mining area and its adjacent region are primarily composed of sea–land interaction deposition, with a maximum deposition thickness of up to 1.3 km. We observed that the low-velocity anomalies in the shallow surface layer (< 1.2 km) in the Baiyuan, Anyuan, and Gaokeng mine areas are particularly significant, which may be caused by coal mining activities. Because the presence of coalmine gob area and coalbed methane production during coal mining can slow down the shear wave velocity. Additionally, the low-velocity anomalies observed around the AYF and WKF zones extend to depths of approximately 3 km (Figs. 11 and
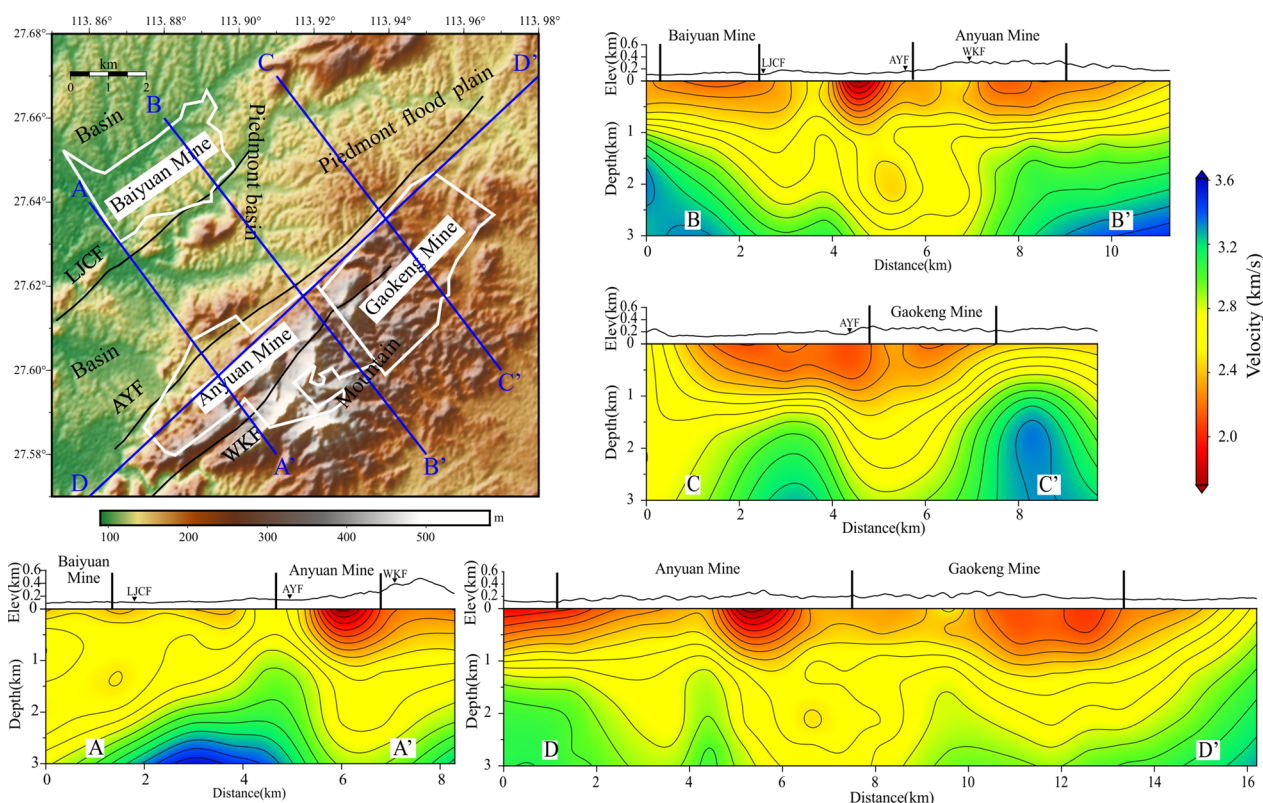
Gong *et al. Earth, Planets and Space*   (2023) 75:129

Page 13 of 15

Fig. 12 Selected vertical profiles locations and their shear wave velocity distributions: **a** AA′, **b** B-B′, **c** C–C′ and **d** D-D′

12), which could be associated with fracture media and the presence of oil and gas in the fault zone. The top coal mining area is often composed of swamp facies or tidal flat facies mudstone and silty mudstone, which has a strong sealing ability for coal reservoirs (Qiu and Li 2019). Consequently, the oil and gas produced during coal mining could migrate into the faults and gaps between the fault zones, resulting in low-velocity anomalies in the shear wave.

Conclusion

We collected about 1 month of seismic data recorded by a local dense array and applied direct surface-wave tomography to image the high-resolution shallow crustal shear wave structure around the Anyuan mining area and its adjacent region of Pingxiang City, Jiangxi Province in South China. The results show that the basins and piedmont basins areas presented low-velocity anomalies, while the uplifted mountainous areas without coal mining exhibited high-velocity anomalies. Influenced by the sedimentary structural depressions and coal mining activities, the mining areas exhibited significant low-velocity anomalies in the shallow surface (< 1.2 km). Specifically,

the AYF and WKF zones exhibited low-velocity anomalies from the ground surface to a depth of ~3 km underground. The low-velocity anomalies at depths less than 1.2 km could be related to the sedimentary environment of coal mines and the coal mining activities, while the low-velocity anomalies at depths below 1.2 km were caused by the presence of fracture medium, oil and gas in the faults zone. Furthermore, the result also revealed the AYF inclined towards the northwest and extended to a depth of ~3 km underground. In summary, our results agreed well with the topography and regional geological structure of the study areas, which could reveal information on the coal seam distribution, coal mining activity, and fault geometry to a certain extent.

Abbreviations

ANT	Ambient noise tomography
AYF	Anyuan fault
WKF	Wangkeng fault
LJCF	Luojiachong fault
CCFs	Cross-correlation functions
EGFs	Empirical green functions
SNR	Signal-to-noise
STD	Standard deviation of residual error

Gong *et al. Earth, Planets and Space*   (2023) 75:129

Page 14 of 15

Availability of data and materials
The datasets and code used during the current study are available from the corresponding authors on reasonable request.

Declarations

Ethics approval and consent to participate
Not applicable.

Consent for publication
Not applicable.

Competing interests
The authors declare that they have no competing interests.

Author details
[1]State Key Laboratory of Nuclear Resources and Environment, East China University of Technology, Nanchang 330013, China. [2]State Key Laboratory of Geological Processes and Mineral Resources, China University of Geosciences, Beijing 10008, China. [3]Jiangxi Earthquake Agency, Nanchang 330026, China. [4]East China University of Technology, Nanchang 330013, China. [5]School of Geophysics and Geomatics, China University of Geosciences, Wuhan 430074, China. [6]Beijing Earthquake Agency, Beijing 10008, China.

References
Aster RC, Borchers B, Thurber CH (2013) Parameter estimation and inverse problems. Academic press, Burlington

Bensen GD, Ritzwoller MH, Barmin MP, Levshin AL, Lin F, Moschetti MP, Shapiro NM, Yang Y (2007) Processing seismic ambient noise data to obtain reliable broad-band surface wave dispersion measurements. Geophys J Int 169(3):1239–1260

Bensen GD, Ritzwoller MH, Shapiro NM (2008) Broadband ambient noise surface wave tomography across the United States. J Geophys Res Solid Earth 113:B05306

Brocher TM (2005) Empirical relations between elastic wavespeeds and density in the Earth's crust. Bull Seismol Soc Am 95(6):2081–2092

Campillo M, Paul A (2003) Long-range correlations in the diffuse seismic coda. Science 299(5606):547–549

Cassereau D, Fink M (1992) Time-reversal of ultrasonic fields-Party III: theory of the closed time-reversal cavity. IEEE Trans Ultrason Ferroclectr Freq Control 39(5):579–592

Deng R, Xu B, Zhang L, Li R, Gao Y, Yang H, Du Y (2005) Assessment of the hydrocarbon source rocks in upper Paleozoic-Lower Triassic in West Ping depression. Nat Gas Ind 25(3):23–28

Dziewonski A, Bloch S, Landisman M (1969) A technique for the analysis of transient seismic signals. Bull Seismol Soc Am 59(1):427–444

Ekström G, Abers GA, Webb SC (2009) Determination of surface-wave phase velocities across US Array from noise and Aki's spectral formulation. Geophys Res Lett 36:L18301

Fang H, Zhang H (2014) Wavelet-based double-difference seismic tomography with sparsity regularization. Geophys J Int 199(2):944–955

Fang H, Yao H, Zhang H, Huang YC, van der Hilst RD (2015) Direct inversion of surface wave dispersion for three-dimensional shallow crustal structure based on ray tracing: methodology and application. Geophys J Int 201(3):1251–1263

Gu N, Wang K, Gao J, Ding N, Yao H, Zhang H (2019) Shallow crustal structure of the Tanlu Fault Zone Near Chao Lake in Eastern China by direct surface wave tomography from local dense array ambient noise analysis. Pure Appl Geophys 176:1193–1206

Hansen PC (2007) Regularization tools version 4.0 for Matlab 7.3. Numer Algorithms 46:189–194

Herrmann RB (2013) Computer programs in seismology: an evolving tool for instruction and research. Seismol Res Lett 84(6):1081–1088

Herrmann RB, Ammon CJ (2002) Computer Programs in Seismology: Surface Waves, Receiver Functions and Crustal Structure, Version 330 St Louis. Saint Louis University, St Louis

Huang YC, Yao H, Huang BS, van der Hilst RD, Wen KL, Huang WG, Chen CH (2010) Phase velocity variation at periods of 05–3 seconds in the Taipei Basin of Taiwan from correlation of ambient seismic noise. Bull Seismol Soc Am 100(5A):2250–2263

Huang Y, Zha H, Gao J, Linghu J, Xuan J, Zhou J, Dong R, Huo J, Zhang H (2021) Predicting the distribution of coalbed methane by ambient noise tomography with a dense seismic array. Chineese J Geophys 64(11):3997–4011

Li H, Zhang L, Liang F, Yang H, Gao S (2003) The marine petroleum system characteristics of Pingle depression in Jiangxi Province. Xinjiang Petrol Geol 24(3):210–213

Li H, Su W, Wang C, Huang Z (2009) Ambient noise Rayleigh wave tomography in western Sichuan and eastern Tibet. Earth and Planet Sci Lett 282(1–4):201–211

Li H, Bernardi F, Michelini A (2010) Surface wave dispersion measurements from ambient seismic noise analysis in Italy. Geophys J Int 180(3):1242–1252

Li H, Li S, Song XD, Gong M, Li X, Jia J (2012) Crustal and uppermost mantle velocity structure beneath northwestern China from seismic ambient noise tomography. Geophys J Int 188(1):131–143

Li H, Zhao F, Zhao F, Mao Y (2015) Three dimensional velocity structure seismic tomography of up-crust in Jiangxi province. Prog Geophys 30(3):1049–1055

Li Z, Ni S, Zhang B, Bao F, Zhang S, Deng Y, Yuen DA (2016a) Shallow magma chamber under the Wudalianchi Volcanic Field unveiled by seismic imaging with dense array. Geophys Res Lett 43(10):4954–4961

Li C, Yao H, Fang H, Huang X, Wan K, Zhang H, Wang K (2016b) 3D near-surface shear-wave velocity structure from ambient-noise tomography and borehole data in the Hefei urban area. China Seismol Res Lett 87(4):882–892

Li F, Zhang C, Chen A, Pan B, Xiong C, Li B (2016c) Sedimentary environment and coal formation model of Anyuan arear in Pingxiang Depression. Sci Technol Eng 16(23):114–118

Lin FC, Ritzwoller MH, Townend J, Bannister S, Savage MK (2007) Ambient noise Rayleigh wave tomography of New Zealand. Geophys J Int 170(2):649–666

Lin FC, Moschetti MP, Ritzwoller MH (2008) Surface wave tomography of the western United States from ambient seismic noise: Rayleigh and love wave phase velocity maps. Geophys J Int 173(1):281–298

Lin FC, Li D, Clayton RW, Hollis D (2013) High resolution 3D shallow crustal structure in Long Beach, California: application of ambient noise tomography on a dense seismic array Noise tomography with a dense array. Geophysics 78(4):Q45–Q56

Liu D, Chen F (2021) Analysis of surface movement deformation in Anyuan colliery. Jiangxi Coal Sci Technol 1:107–110

Liu X, Zhong D, Yuan J, Xie Q, Li Y (2004) Tectonic characteristics in the Pingxiang area in the junction belt between the Yangtze plate and South China plate. J Geomech 10(4):372–379

Liu Y, Zhang H, Fang H, Yao H, Gao J (2018) Ambient noise tomography of three-dimensional near-surface shear-wave velocity structure around the

Gong *et al. Earth, Planets and Space*   (2023) 75:129

Page 15 of 15

hydraulic fracturing site using surface microseismic monitoring array. J Appl Geophys 159:209–217

Luo Y, Yang Y, Xu Y, Xu H, Zhao K, Wang K (2015) On the limitations of interstation distances in ambient noise tomography. Geophys J Int 201(2):652–661

Luo S, Yao H, Li Q, Wang W, Wan K, Meng Y, Liu B (2019) High-resolution 3D crustal S-wave velocity structure of the middle-lower Yangtze river Metallogenic Belt and implications for its deep geodynamic setting. Sci China Earth Sci 62(9):1361–1378

Paige CC, Saunders MA (1982a) LSQR: an algorithm for sparse linear equations and sparse least squares. ACM Trans Math Softw 8(1):43–71

Paige CC, Saunders MA (1982b) Algorithm 583: LSQR: Sparse linear equations and least squares problems. ACM Trans Math Softw 8(2):195–209

Qiu K, Li L (2019) Preliminary analysis of resource potential of coalbed methane of Pingle depression, Jiangxi. Jiangxi Coal Sci Technol 2:4–6

Rawlinson N, Sambridge M (2004) Wave front evolution in strongly heterogeneous layered media using the fast marching method. Geophys J Int 156(3):631–647

Sabra KG, Gerstoft P, Roux P, Kuperman WA, Fehler MC (2005) Surface wave tomography from microseism in southern California. Geophys Res Lett 32:L14311

Shapiro NM, Campillo M (2004) Emergence of broadband Rayleigh waves from correlations of the ambient seismic noise. Geophys Res Lett 31:L07614

Shearer PM (2009) Introduction to seismology. Cambridge University Press, Cambridge

Shen Y, Ren Y, Gao H, Savage B (2012) An improved method to extract very-broadband empirical green functions from ambient seismic noise. Bull Seismol Soc Am 102(4):1872–1877

Simons FJ, van der Hilst RD, Montagner JP, Zielhuis A (2002) Multimode Rayleigh wave inversion for heterogeneity and azimuthal anisotropy of the Australian upper mantle. Geophys J Int 151(3):738–754

Simons FJ, Loris I, Nolet G, Daubechies IC, Voronin S, Judd JS, Vetter PA, Charléty J, Vonesch C (2011) Solving or resolving global tomographic models with spherical wavelets, and the scale and sparsity of seismic heterogeneity. Geophys J Int 187(2):969–988

Stehly L, Campillo M, Shapiro NM (2007) Traveltime measurements from noise correlation: stability and detection of instrumental time-shifts. Geophys J Int 171(1):223–230

Tan X, Yang R, Mo S, Liu X (2001) Research about coal controlling structures in Jiangxi Pingxiang mining area. Hunan Geology 20(3):168–184

Wang J, Yao H, Wang W, Wang B, Li C, Wei B, Feng L (2018) Study of the near-surface velocity structure of the Hutubi gas storage area in Xinjiang from ambient noise tomography. Chin J Geophys 61(11):4436–4447

Wessel P, Smith WH (1995) New version of the generic mapping tools. Eos Trans AGU 76(33):329–329

Xi Y, Ouyang N, Xu Y, Huang H (1999) The research progress of the deposition of Anyuan Group in Pingle depression in Jiangxi. GeoSci Front 6:173–174

Xiao F (2020) Geological characteristics of coalbed methane in Anyuan Formation in Pingxiang mining area. Jiangxi Coal Sci Technol 4:167–173

Xie T, Xu T, Ai Y, Zeng Q, Zhang W, Zheng F (2021) Imaging the shallow crustal velocity structure of the Qingchengzi ore field on the Liaodong Peninsula, China, with a short-period dense array using ambient noise tomography. Tectonophysics 813:228913

Yang Y, Ritzwoller MH, Levshin AL, Shapiro NM (2007) Ambient noise Rayleigh wave tomography across Europe. Geophys J Int 168(1):259–274

Yao H, van der Hilst RD, de Hoop MV (2006) Surface wave array tomography in SE Tibet from ambient seismic noise and two-station analysis—I. Phase Velocity Maps Geophys J Int 166(2):732–744

Yao H, Beghein C, Hilst R (2008) Surface wave array tomography in SE Tibet from ambient seismic noise and two-station analysis—II. Crustal and upper-mantle structure. Geophys J Int 173(1):205–219

Yao H, Gouedard P, Collins JA, Mcguire JJ, Hilst R (2011) Structure of young East Pacific Rise lithosphere from ambient noise correlation analysis of fundamental and higher-mode Scholte-Rayleigh waves. C R Geosci 343(8–9):571–583

Yu G, Xu T, Liu J, Ai Y (2020) Late Mesozoic extensional structures and gold mineralization in Jiaodong Peninsula, eastern North China Craton: the inspiration from ambient noise tomography with a dense seismic array. Chin J Geophys 63(t):1878–1893

Zhan Z, Clayton RW (2010) Apparent velocity change caused by temporal variation of frequency content of ambient seismic noise. AGU Fall Meet Abstr 2010:S21D – S28

Zhang P, Deng Q, Zhang Z, Li H (2013) Active faults, earthquake hazards and associated geodynamic processes in continental China (in Chinese). Scientia Sinica Terrae 43(10):1607–1620

Zhang B, Li Z, Bao F, Deng Y, You Q, Zhang S (2016) Shallow shear-wave velocity structures under the Weishan volcanic cone in Wudalianchi volcano field by microtremor survey. Chin J Geophys 59(10):3662–3673

Zheng S, Sun X, Song X, Yang Y, Ritzwoller MH (2008) Surface wave tomography of China from ambient seismic noise correlation. Geochem Geophys Geosyst 9:Q05020

Zheng Y, Shen W, Zhou L, Yang Y, Xie Z, Ritzwoller MH (2011) Crust and uppermost mantle beneath the North China Craton, northeastern China, and the Sea of Japan from ambient noise tomography. J Geophys Res 116:B12312

Publisher's Note